

BaAs₃: A narrow gap 2D semiconductor with vacancy-induced semiconductor-metal transition

Ping Tang,¹⁺ Jun-Hui Yuan,¹⁺ Ya-Qian Song,¹ Ming Xu,¹ Kan-Hao Xue,^{1,2*} and Xiang-Shui Miao¹

¹Wuhan National Research Center for Optoelectronics, School of Optical and Electronic Information, Huazhong University of Science and Technology, Wuhan 430074, China

²Univ. Grenoble Alpes, Univ. Savoie Mont Blanc, CNRS, Grenoble INP, IMEP-LAHC, 38000 Grenoble, France

⁺The authors P. Tang and J.-H. Yuan contributed equally to this work.

Corresponding Author

*E-mail: xkh@hust.edu.cn (K.-H. Xue)

ABSTRACT: Searching for novel two-dimensional (2D) materials is highly desired in the field of nanoelectronics. We here propose a new 2D crystal barium tri-arsenide (BaAs₃) with a series of encouraging functionalities. Being kinetically and thermally stable, the monolayer and bilayer forms of BaAs₃ possess narrow indirect band gaps of 0.87 eV and 0.40 eV, respectively, with high hole mobilities on the order of $\sim 10^3$ cm² V⁻¹ s⁻¹. The electronic properties of 2D BaAs₃ can be manipulated by controlling the layer thickness. The favorable cleavage energy reveals that layered BaAs₃ can be produced as a freestanding 2D material. Furthermore, by introducing vacancy defects monolayer BaAs₃ can be transformed from a semiconductor to a metal. 2D BaAs₃ may find promising applications in nanoelectronic devices.

KEYWORDS: 2D materials, barium triarsenide, monolayer BaAs₃, carrier mobility, electronic properties, vacancy defect, density functional theory

Two-dimensional (2D) materials, such as graphene, transitional metal dichalcogenides (TMDCs) and phosphorene, hold great application potential for nanoelectronics, optoelectronics, energy storage and catalysis [1–12]. For example, monolayer black phosphorus or phosphorene, with a desired direct band gap of 2.0 eV, as well as a high hole mobility of about $1.14 \times 10^3 \text{ cm}^2 \text{ V}^{-1} \text{ s}^{-1}$ - $2.60 \times 10^4 \text{ cm}^2 \text{ V}^{-1} \text{ s}^{-1}$, has been considered a strong candidate for next generation high performance field effect transistors [10,13]. However, the weak chemical stability under ambient conditions and the low electron mobility still hinder its practical application. Nowadays, searching for novel 2D materials with unique structural and desired electronic properties is still an active area of research.

Very recently, a series of 2D pnictides (nitrides, phosphides and arsenides) semiconductors have been theoretically proposed as novel 2D semiconductors with high carrier mobilities ($\sim 10^3 \text{ cm}^2 \text{ V}^{-1} \text{ s}^{-1}$ - $10^5 \text{ cm}^2 \text{ V}^{-1} \text{ s}^{-1}$) that are comparable or superior to those of phosphorene [14–25]. For instance, in monolayer Pt₂N₄ with a planar penta-structure, the electron mobility at room temperature can reach $1.1 \times 10^5 \text{ cm}^2 \text{ V}^{-1} \text{ s}^{-1}$, comparable to that in graphene [20]. In addition to the materials with a single atomic layer thickness, such as TM₂X₄(TM=Ni, Pd and Pt, X=P, As) [23], most of them possess blue phosphorene-type or black phosphorene-type structural features. For example, CaP₃(CaAs₃) monolayers possess similar 2D networks of puckered configurations, and

the puckered polyanionic P_3^2 (As_3^{2-}) nets are derivatives of the black phosphorene (puckered arsenene) structure by removing 1/4 of the P (As) atoms. Moreover, bulk barium triarsenide ($BaAs_3$), also a member of CaP_3 families as $CaAs_3$, SrP_3 and $SrAs_3$, was first synthesized in 1981 [26]. Although known for decades, the research on $BaAs_3$ has been very rare. Recently, the bulk CaP_3 family has been predicted to be topological nodal-line semimetals [27], which may open a new research aspect for these materials. Compared with CaP_3 and $CaAs_3$, which belong to a low symmetry ($P-1$ or $C-1$), $BaAs_3$ has a higher space group symmetry $C2/m$. The stacking structural feature of $BaAs_3$ is similar to CaP_3 or $CaAs_3$, while CaP_3 and $CaAs_3$ were predicted to be stable when attenuated to atomic layer thickness, and exhibiting extraordinary optoelectronic properties. Thus, two questions are naturally raised. (i) Is $BaAs_3$ film of the atomic layer thickness stable? (ii) Given that few-layer $BaAs_3$ can be fabricated as free-standing 2D material, what about its electronic structure?

To answer these questions, in this work we have systematically investigated the stability and electronic properties of bulk $BaAs_3$ and freestanding monolayer $BaAs_3$. First, the kinetic and thermodynamic stabilities of monolayer $BaAs_3$ are confirmed according to phonon dispersion and high temperature molecular dynamics simulation. Then, we shall investigate the band gaps, carrier mobilities, and optical absorption characteristics of monolayer and few-layer $BaAs_3$. In particular, a detailed study of the vacancy defects in monolayer $BaAs_3$ with various concentrations have been carried out by employing the self-energy corrected shell GGA-1/2 method.

Computational Methods

We performed density functional theory (DFT) calculations using plane-wave-based Vienna *Ab-initio* Simulation Package (VASP) [28,29]. The generalized gradient approximation (GGA) within the Perdew-Burke-Ernzerhof (PBE) [30] functional form was used for the exchange-correlation energy, and projector augmented-wave pseudopotentials [31,32] were used to replace the core electrons. The valence electron configurations of Ba and As are $5s, 5p, 6s$ and $4s, 4p$, respectively. The screened exchange hybrid functional HSE06 [33] was used to calculate the electronic band structures in order to rectify the band gaps in GGA-PBE. The plane wave kinetic energy cutoff was fixed to be 500 eV. The van der Waals interactions were corrected by the DFT-D3 approach [34]. During structural relaxations, the convergence criterion for total energy was set to 1.0×10^{-6} eV, and structural optimization was obtained until the Hellmann-Feynman force acting on any atom was less than 0.01 eV/Å in each direction. The phonon dispersion was calculated with the density functional perturbation theory, using the PHONOPY code [35]. *Ab initio* molecular dynamics (AIMD) simulations were performed to examine the thermal stability of the structures, where NVT canonical ensembles were used [36].

While the screened exchange hybrid functional HSE06 is well-known for its high quality electronic structure results, the slow convergence of the Hartree-Fock part yields much higher computational load than conventional GGA. In order to investigate the electronic structures of defects, where large supercells are used, we also implemented the shell GGA-1/2 method (shGGA-1/2) for self-energy correction [37].

The method is a variant of the original GGA-1/2 method proposed by Ferreira and coworkers in 2008 [38], with focus on better treatment of the covalent bonding. Self-energy correction was carried out on the As anions, where the inner and outer cutoff radii for the As self-energy potential [39] were fixed in a variational way, where the optimal set of cutoff radii should maximize the band gap.

Results and discussion

Geometric structures

The symmetry of bulk barium triarsenide (BaAs_3) is monoclinic with space group $C2/m$, with the optimized structure shown in **Fig.1a-c**. Bulk BaAs_3 has a 2D network of puckered configurations in-plane, and different van der Waals layers stacking out-of-plane. The puckered polyanionic As_3^{2-} nets derive from the grey arsenene structure, with a quarter of As atoms missing, similar to CaAs_3 [19]. Our optimized lattice parameters of bulk BaAs_3 obtained using the D3-Grimme correction are $a = 10.22 \text{ \AA}$, $b = 7.82 \text{ \AA}$, $c = 6.06 \text{ \AA}$, and $\beta = 113.70^\circ$, which is in good accordance with the experimental results ($a = 11.16 \text{ \AA}$, $b = 7.76 \text{ \AA}$, $c = 6.01 \text{ \AA}$ and $\beta = 113.55^\circ$) [26]. We also examined the electronic properties of bulk BaAs_3 based on GGA-PBE and HSE06 calculations, with or without considering the effect of spin-orbit coupling (SOC). As shown in **Fig. 1d**, regardless of the functional used, bulk BaAs_3 is a semimetal when SOC is neglected. In addition, the semimetallic nature is retained when SOC is considered (see band structures in **Fig. S1**).

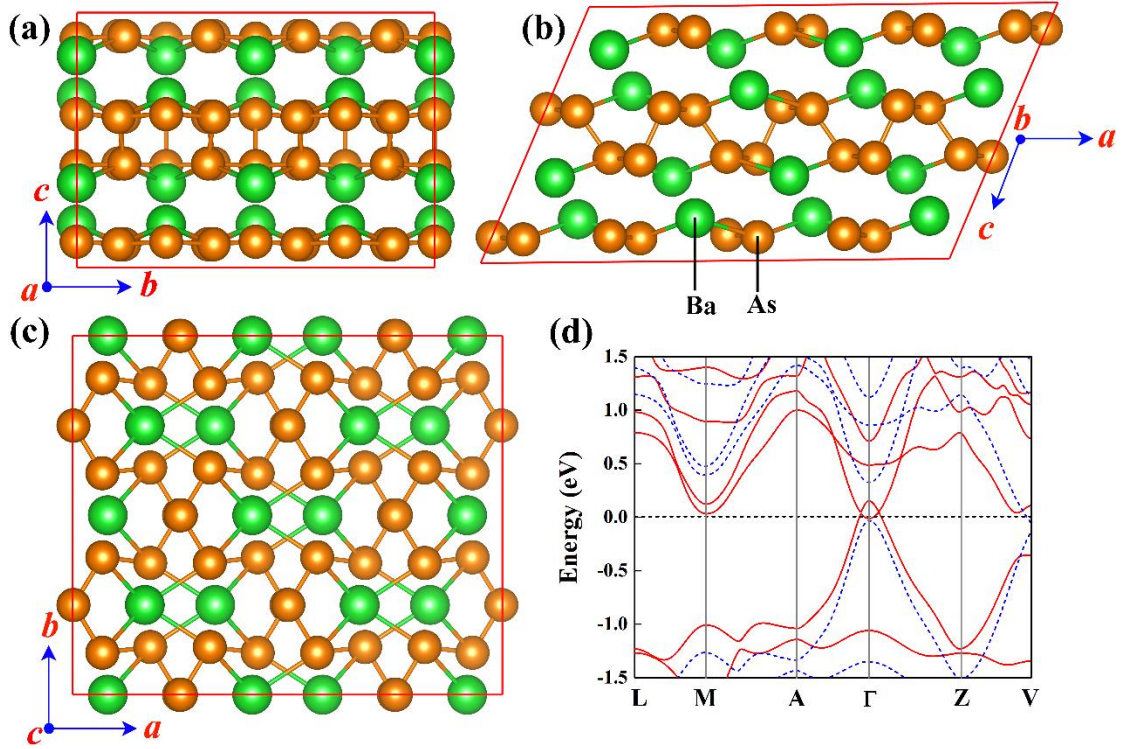


Figure 1 (a,b,c) Crystal structure of optimized bulk BaAs₃, showing a 2×2×2 supercell from three distinct perspectives. The green and brown ball represent Ba and As atoms, respectively. (d) Calculated electronic band structures of bulk BaAs₃ using GGA-PBE (solid red line) and HSE06 (dash blue line), respectively. The Fermi levels are set to zero energy.

When exfoliating from the bulk, monolayer (ML for short) BaAs₃ has in theory the same geometric structures with high stability, as plotted in [Fig. 2a](#). The optimized lattice parameters of ML BaAs₃ are $a = 6.51 \text{ \AA}$, $b = 6.25 \text{ \AA}$ and $\gamma = 73.19^\circ$. The As-As bond length ranges from 2.48 \AA to 2.53 \AA , similar to that of puckered arsenene (2.485 \AA to 2.501 \AA) [40], while the Ba-As bond length is from 3.24 \AA to 3.82 \AA . Compared with the bulk phase, however, a slight distortion for As-As bond length (2.48 \AA to 2.49 \AA for bulk) and Ba-As bond length (3.29 \AA to 3.79 \AA for bulk) have been found in the

ML form. Hence, careful theoretical verification is still required for the stability of the proposed ML BaAs₃ structure.

First of all, we evaluate the feasibility of exfoliating the ML BaAs₃ sheet from its layered bulk crystal, from a cleavage energy aspect. A five-layer BaAs₃ slab is utilized to server as a model of the bulk. The computed cleavage energy is 1.02 J m⁻², as illustrated in **Fig. 2c**. The DFT-estimated exfoliation energy of ML BaAs₃ is larger than that of graphite (0.37 J m⁻² from experimental and 0.32 J m⁻² in theory) [41,42] but at the same level of InP₃ (1.32 J m⁻²) [14], GeP₃ (1.14 J m⁻²) [15], CaP₃ (1.30 J m⁻²) [18] and CaAs₃(1.36 J m⁻²) [19]. Therefore, in principle ML BaAs₃ crystal could be prepared experimentally from its bulk counterpart using mechanical cleavage or liquid phase exfoliation. Subsequently, we focus on the kinetic stability and thermal stability, which are crucial for real experimental fabrication. The kinetic stability was assessed by calculating the phonon dispersion relations. As shown in **Fig. 2d**, no imaginary phonon modes are identified, indicating that ML BaAs₃ is kinetically stable. The highest phonon mode of ML BaAs₃ is 237 cm⁻¹, which is comparable to that of puckered arsenene (253 cm⁻¹) [40]. In addition, the mode stems from the As-As bond, as revealed by the phonon density of states results (**Fig. 2d**). Furthermore, the thermodynamic stability of ML BaAs₃ was assessed by performing AIMD simulations. As pointed out by the structural snapshots and variations of total energy in **Fig. S2**, ML BaAs₃ maintains its structure up to 500 K within 10 ps, with no geometric reconstruction or bond breaking discovered during the whole process. Combining the results from cleavage energy, phonon dispersion as well as high temperature AIMD, we conclude that ML BaAs₃ can be

exfoliated from the bulk crystal, staying as a freestanding 2D material.

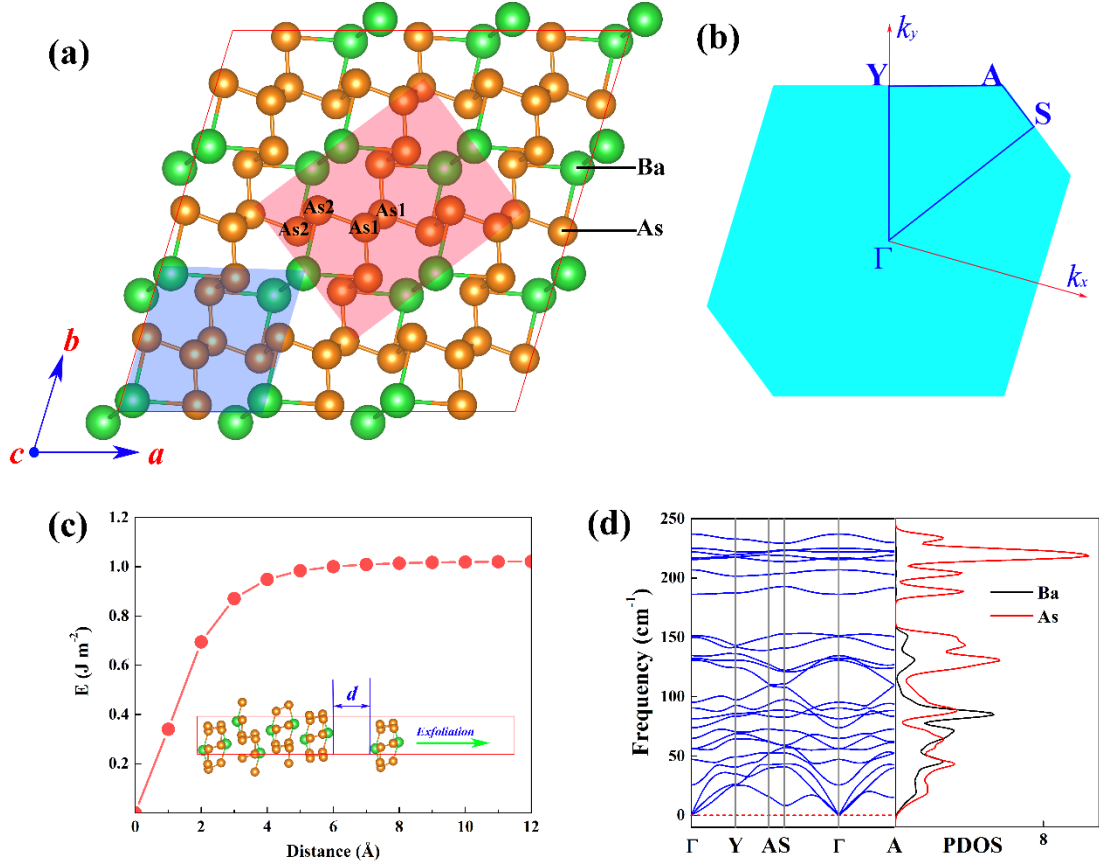


Figure 2 (a) Top view of the optimized ML BaAs₃ in a 3×3 supercell. The light blue and light red areas denote the primitive cell and the corresponding rectangular cell of ML BaAs₃, respectively. (b) The corresponding first Brillouin zone of ML BaAs₃ primitive cell with high symmetry points marked. (c) Cleavage energy estimation for the formation of ML BaAs₃, calculated by enlarging the interlayer distance between the ML system that is removed from the remainder of a five-layer slab. (d) Calculated phonon dispersion spectra and phonon density of states of the ML BaAs₃.

Electronic properties

To understand the bonding characteristics of ML BaAs₃, we calculated its electron localization function (ELF) [43,44] and Bader charges [45–47]. As shown in **Fig. S3**, the ionic and covalent characters for Ba-As and As-As bonds, respectively, are clearly

demonstrated through ELF analysis. Interestingly, ELF and Bader charge analysis (results summarized in [Table S1](#)) reveal there are two different types of As in BaAs₃, As1 connected by As-As bonds only and As2 connected by both Ba-As and As-As bonds, respectively. About 1.32|e| charge on average has been transferred from the Ba atom to the neighboring As2 atoms ($\sim 0.56\text{-}0.57$ |e|), while the As1 atom in the As-As bond gains a low amount of charge (~ 0.18 |e|). The As-As bond in ML BaAs₃ is much different from that of puckered arsenene, whose As atoms in the As-As bonds are almost all neutral ($\sim 0.025/0.033$ |e|), as shown in [Fig. S4b](#). In sum, the hybrid ionic and covalent bonds between Ba and As atoms are jointly responsible for the formation and stability of the ML BaAs₃.

Subsequently, we focus on the energy band structure of ML BaAs₃. Heavy elements like As may render strong spin-orbit coupling (SOC) effect. Hence, we calculate band structures of ML BaAs₃ both with and without considering SOC, using either the PBE functional or the HSE06 hybrid functional. Meanwhile, the new shGGA-1/2 self-energy correction method is also used in band structure calculations for comparison. As shown in [Figure 3a](#), using GGA-PBE without turning on SOC, the ML BaAs₃ is predicted to be an indirect semiconductor with a narrow band gap value of 0.16 eV. The valence band maximum (VBM) is located at the Γ -point while the conduction band minimum (CBM) lies along the S - Γ direction, closer to the S point. Similar band structures but with larger band gap values of 0.75 eV/0.87 eV have been confirmed based on HSE06/shGGA-1/2 calculations, respectively. We then examine the effect of SOC in our calculations. The CBM and VBM of ML BaAs₃ do not show

discernable shift after turning on the SOC, regardless of using PBE or HSE06, as plotted in [Fig.S5](#). The SOC effect produces less than 0.01 eV variation in the band gap. Therefore, we shall neglect the SOC effect in all forthcoming band structure calculations. Furthermore, the partial density of states (PDOS) results show that the As-4p (especially the As2-4p) states dominate the orbit contribution around the Fermi level, which is further confirmed by the spatial charge distributions of VBM and CBM (shown in [Figs. 3b and 3c](#)).

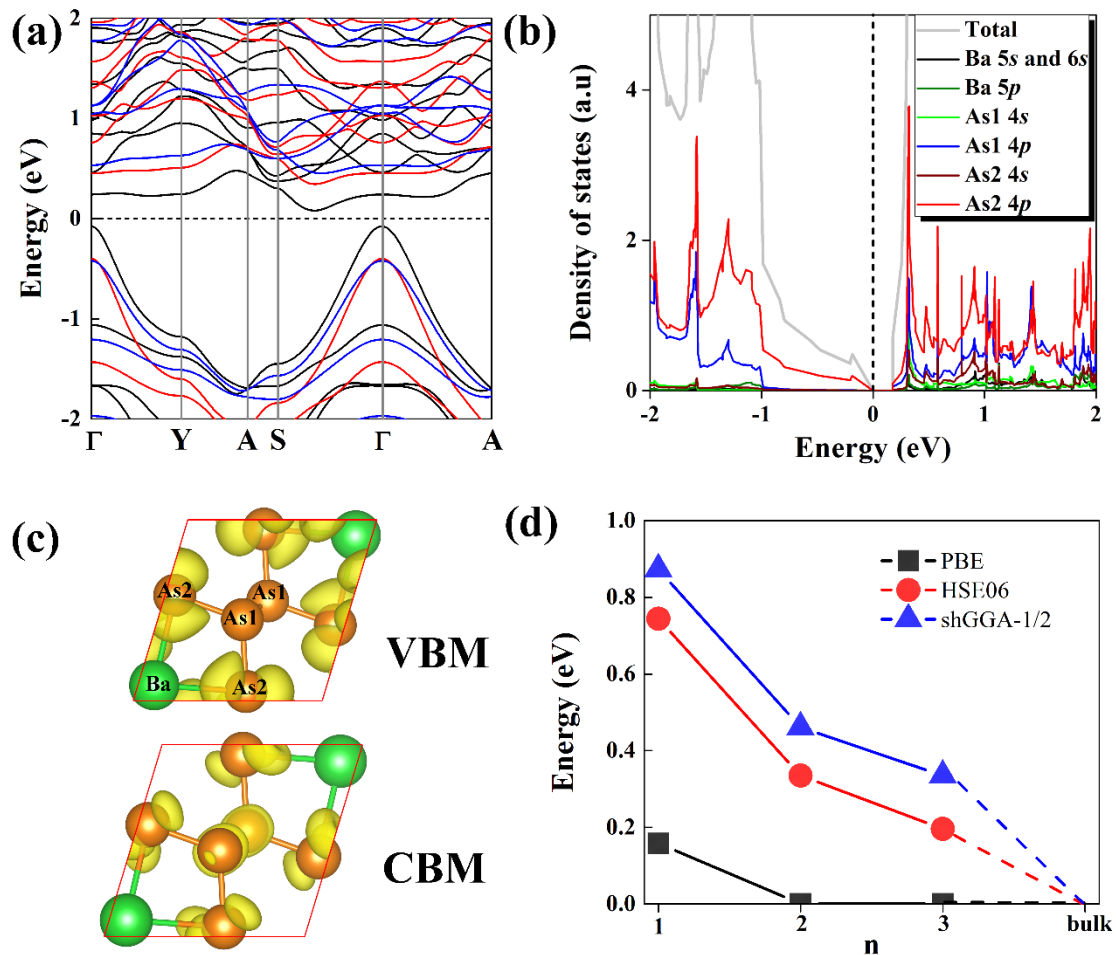


Figure 3 (a) Electronic band structures of ML BaAs₃ calculated using GGA-PBE (solid black line), HSE06 (solid red line) and shGGA-1/2 (solid blue line) without considering SOC. (b) Partial DOS of the ML BaAs₃ calculated using the PBE functional. (c) Spatial distribution of the wave-functions corresponding to the VBM and CBM of ML BaAs₃

(contour density: $0.02 \text{ e } \text{\AA}^{-3}$). (d) Computed band gaps of BaAs_3 multilayers versus the number of atomic layers, using GGA-PBE, HSE06 hybrid functional and shGGA-1/2, respectively.

The ML BaAs_3 owns a narrow band gap while the bulk BaAs_3 is calculated to be a semimetal. In order to elucidate the changes in the electronic properties of BaAs_3 from the bulk to few layers, we have investigated the electronic band gaps of 2D BaAs_3 with varying number of layers, with the results shown in [Fig. 3d](#) and [Fig. S6](#). The electronic structures of 2D BaAs_3 multilayers indeed strongly depend on the number of layers. At the PBE level, ML BaAs_3 is the only semiconductor while bilayer (BL for short) and tri-layer (TL for short) BaAs_3 remain metallic. According to both HSE06 and shGGA-1/2 calculations, 2D BaAs_3 up to 3 layers can still maintain the indirect band gap feature ([Fig.S6](#)), though the band gap is diminished for more layers. For BL BaAs_3 , the indirect band gap is 0.33 eV/0.40 eV (HSE06/shGGA-1/2), while the TL BaAs_3 possesses an indirect band gap of 0.20 eV/0.34 eV (HSE06/shGGA-1/2). Therefore, the band gap of BaAs_3 can be engineered by controlling the layer thickness to cover a relatively large range of 0-0.75 eV/0-0.87 eV (HSE06/shGGA-1/2). Detailed optimized lattice constants of BL, TL and bulk BaAs_3 are shown in [Table S2](#).

Carrier Mobility

The ML BaAs_3 exhibits a narrow band gap close to that of germanium (0.74 eV)[37], suggesting it may find potential application in electronic devices. Therefore,

we systematically calculated the carrier mobilities (for electrons and holes) of ML and BL BaAs₃ based on the deformation potential theory of Bardeen and Shockley [48]. For 2D semiconductors, Lang *et al.* [49] recently gave a new formula for the acoustic phonon-limited mobility, taking into account the anisotropic elastic constants or deformation potential constants. For nonisotropic 2D materials, the theoretical carrier mobility can be calculated by the following equation [42,49,50]

$$\mu_{2D} = \frac{e\hbar^3 \left(\frac{5C_a^{2D} + 3C_b^{2D}}{8} \right)}{k_B T (m_a)^{\frac{3}{2}} (m_b)^{\frac{1}{2}} \left(\frac{9E_{1a}^2 + 7E_{1a}E_{1b} + 4E_{1b}^2}{20} \right)^2},$$

where \hbar is the reduced Planck constant, k_B is the Boltzmann constant, m^* is the effective mass in the direction of transport, m_d is the average effective mass determined by $m_d = (m_a^* m_b^*)^{1/2}$, and T is the temperature ($T = 300$ K). The elastic modulus C_{2D} of the longitudinal strain in the propagation direction is derived from $(E - E_0) / S_0 = C_{2D} (\Delta l / l_0)^2 / 2$, where E is the total energy of the 2D structure, and S_0 is the lattice area of the equilibrium supercell. The deformation potential constant E_1^i is defined as $E_1^i = \Delta E_i / (\Delta l / l_0)$. Here ΔE_i is the energy change of the i^{th} band under proper cell compression and dilatation (calculated using a step of 0.5%), l_0 is the lattice constant in the transport direction and Δl is the deformation of l_0 . Notice that the directions a and b for the unit cell of ML BaAs₃ are not perpendicular to each other. Indeed, the γ angle is 73.19° that could not simply be approximated as 90° . Therefore, for ML BaAs₃ we adopt an orthogonal supercell (shown in **Fig.2a**) to calculate the carrier mobility. In this case, we have to re-calculate the corresponding energy band structures based on the orthorhombic supercell, for the sake of deformation potential

constant evaluation. As shown in **Fig.S7**, the obtained band gap value and indirect gap feature using the orthorhombic supercell are in line with the results from the primitive cell. In addition, considering that GGA-PBE calculations do not recover the correct semiconducting nature for BL-BaAs₃, all the following energy band structures are calculated by HSE06 functional (except for elastic modulus, which can be obtained accurately at the PBE level).

Table 1 Calculated effective mass m^* (m_e , HSE06 results), deformation potential constant $|E_1^i|$ (eV, HSE06 results), elastic modulus C_{2D} (N m⁻¹, PBE results), and carrier mobility μ_{2D} (cm² V⁻¹s⁻¹) for ML and BL BaAs₃ along the a and b directions.

Layers	Carrier type	m_a^*	m_b^*	$ E_{1a} $	$ E_{1b} $	C_a^{2D}	C_b^{2D}	μ_a^{2D}	μ_b^{2D}
ML	electron	0.679	0.634	1.415	1.451	24.86	29.52	629.361	580.419
	hole	0.108	0.262	3.872	6.768	24.86	29.52	1030.549	369.646
BL	electron	0.736	0.953	2.314	3.779	60.14	60.14	249.554	151.994
	hole	0.121	0.298	4.299	9.00	60.14	60.14	1464.680	421.586

As summarized in **Table 1**, the carrier effective masses for ML BaAs₃ along the a/b direction are 0.679/0.634 m_e for the electron and 0.108/0.262 m_e for the hole (m_e is the free electron mass), while those for BL BaAs₃ are 0.736/0.953 m_e and 0.121/0.298 m_e , respectively. The hole effective masses are much smaller than that of electrons, which can be expected from the more steep band structures around VBM. The elastic moduli are 24.86/29.52 N m⁻¹ and 60.14/60.14 N m⁻¹ for ML and BL BaAs₃ along the a/b directions, respectively. The deformation potential constants E_1 for the electron of ML

and BL BaAs₃ are both smaller than that of the hole. Based on the above obtained m^* , C_{2D} and E_1 values, we estimated the acoustic phonon-limited mobilities of ML and BL BaAs₃ as 629.361/580.419 and 249.554/151.994 cm² V⁻¹ s⁻¹ along a/b directions, respectively. In contrast to the relatively weak anisotropy of electron mobilities, the hole mobilities show stronger anisotropy with the value of 1030.549/369.646 cm² V⁻¹ s⁻¹ and 1464.680/421.586 cm² V⁻¹ s⁻¹ along a and b directions for ML and BL BaAs₃, respectively. The large anisotropy of hole mobilities mainly stems from the large effective mass and deformation potential constant along the b direction.

Vacancy induced semiconductor-metal transition

Point defects play a crucial role in the properties of materials, especially in electronic and optoelectronic devices. Therefore, it is very important to study the effect of different types of vacancies with various concentrations in theory and experiment. However, it is difficult to directly study point defects by experiments, thus first-principles calculations appear to be an indispensable means.

For this purpose, we perform calculations with varying supercell sizes ($2 \times 2 \times 1$ to $7 \times 7 \times 1$) for a fairly large set of defects. A single Ba/As vacancy is introduced in each supercell, where large supercells (288/392 atoms for $6 \times 6 \times 1/7 \times 7 \times 1$ supercell) lead to low vacancy concentrations. As mentioned above, there are two different types of As atom in BaAs₃. As far as the anion vacancy is concerned, we considered two different As vacancies, V_{As1} and V_{As2} respectively, while only one Ba cation vacancy (V_{Ba}) was considered.

The defect formation energy, for the case of one neutral defect D per supercell, can be defined as [51]

$$E_f [D] = \{E[D] + \mu[D]\} - E_p$$

where $E[D]$ and E_p are the total energies of the supercell with the defect D and the perfect stoichiometric supercell, while $\mu[D]$ represents the chemical potential of D . We chose the Ba and As chemical potentials as in their ground state solid metal (*b.c.c.* Ba) and (*R-3m* As). The relation between the formation energy and the size of the supercell is illustrated in **Figure 4(a)**.

As the size of the supercell goes from $2 \times 2 \times 1$ to $7 \times 7 \times 1$, the formation energies of the three vacancies show a uniform trend of decreasing. $E_f [\text{Ba}]$ drops from 2.60 eV to 2.41 eV, while $E_f [\text{As1}] / E_f [\text{As2}]$ also drops from 1.48 eV/0.63 eV to 1.15 eV/0.15 eV. For the same supercell scale, $E_f [\text{Ba}]$ is always larger than $E_f [\text{As}]$. Among the two different types of V_{As} , V_{As1} shows a quite smaller formation energy than V_{As2} . In $7 \times 7 \times 1$ supercell, $E_f [\text{As2}]$ is merely 0.15 eV. To sum up, in ML BaAs₃ V_{Ba} is difficult to create, while V_{As2} is the most favorable defect.

After evaluating the feasibility of removing a single atom from different sizes of ML BaAs₃, we then turn our attention to the electronic properties of the vacancy-containing systems. The test results do not show any spin-polarized ground state in these defective supercells, so we have disabled spin polarization. The shGGA-1/2 method is utilized for fast and accurate electronic structure calculation, with comparison to conventional GGA. For Brillouin zones, the 32-atom supercells are sampled with a $7 \times 7 \times 1$ Monkhorst-Pack k-point mesh, the 72-atom and 128-atom

supercells with a $5 \times 5 \times 1$ mesh, and the 200-atom, 288-atom, 392 atom supercells with a $3 \times 3 \times 1$ mesh, respectively.

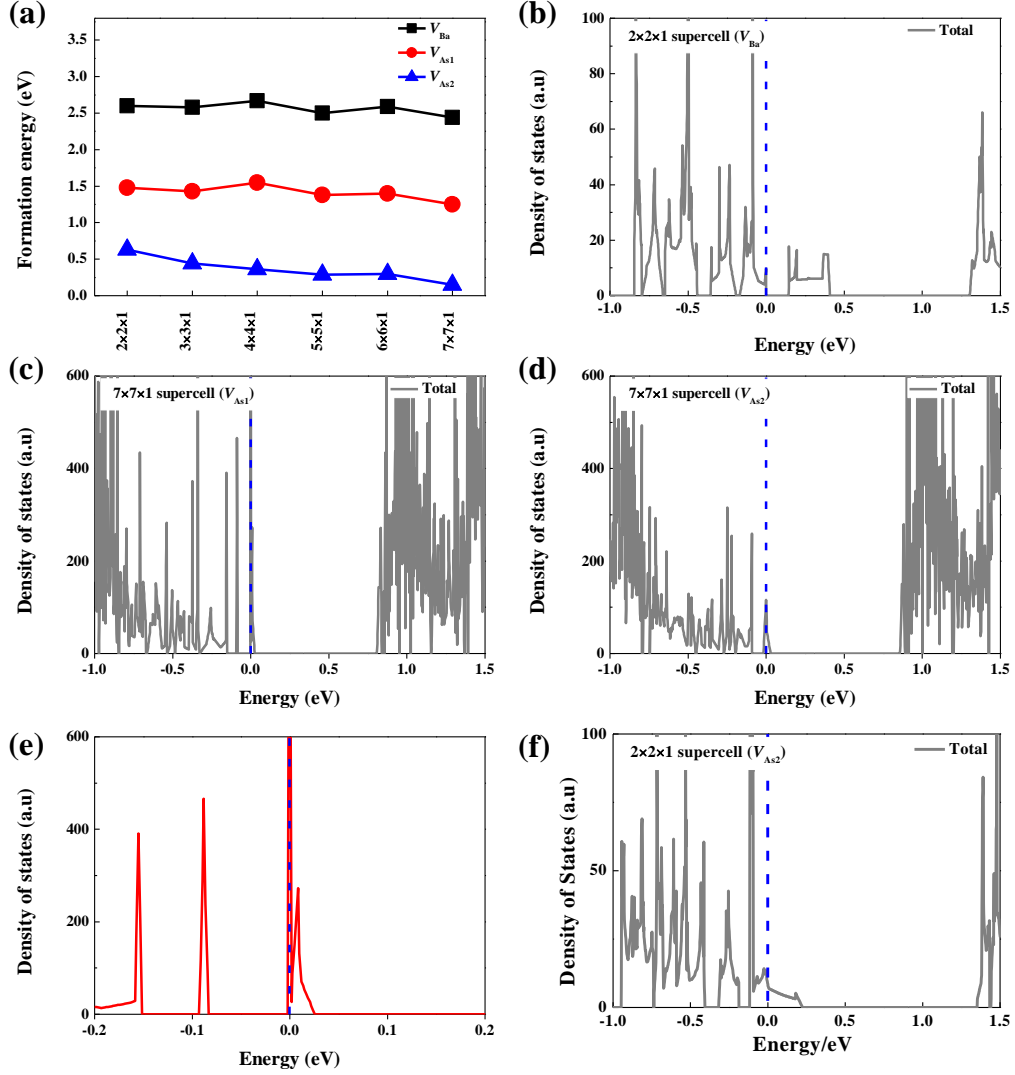


Figure 4 (a) Relation between the defect formation energy and the size of the supercell, for Ba, 1-As and 2-As vacancies. Partial DOS of vacancy-containing supercells calculated using shGGA-1/2: (b) V_{Ba} in a $2 \times 2 \times 1$ supercell; (c) V_{As1} in a $7 \times 7 \times 1$ supercell; (d) V_{As2} in a $7 \times 7 \times 1$ supercell; (e) enlarged view of (c) near the Fermi level; (f) V_{As2} in a $2 \times 2 \times 1$ supercell.

With the vacancy concentration increases, the band gap of V_{Ba} -containing supercell gradually decreases (**Fig. S10**). Yet, even at a very high concentration (3.12% in $2 \times 2 \times 1$ supercell), the cation-deficient ML BaAs₃ still maintains a finite energy gap (**Figure4b**). After introducing V_{Ba} in a $2 \times 2 \times 1$ supercell, the band gap drops from 0.87 eV in perfect supercell to 0.14 eV (both using shGGA-1/2), which suggests that the conductivity of ML BaAs₃ can be adjusted by controlling the V_{Ba} concentration in a quite large range.

Interestingly, the absence of As yields quite different results (**Fig. S11 and Fig. S12**). Both types of V_{As} can transform ML BaAs₃ into a metal at an appropriate concentration. The DOS diagram shows that when the vacancy concentration is high, the density of states near the Fermi level is broadened. On the other hand, in the $7 \times 7 \times 1$ supercell a very sharp but narrow state appears (**Fig. 4c and Fig. 4d**). The hole is highly localized with very tiny dispersion. The ML BaAs₃ can still be regarded as a semiconductor in this sense. Meanwhile, $V_{\text{As}2}$ is much more effective to trigger the semiconductor-metal transition, while it is in the meantime the most ordinary defect as well.

For most semiconductor materials, the conductivity of the material can be enhanced by n-type (typically anion vacancy) or p-type (typically cation vacancy) doping, both of which can convert the material to a metal after reaching a suitable concentration. However, for ML BaAs₃, the incorporation of all three kinds of vacancies only yields p-type conduction. This can be attributed to the unusual stoichiometry of the material, where the As vacancy actually does not act like a true anion vacancy (i.e.,

not inducing n-type conduction). This interesting finding is of great significance for the design of novel electronic devices in many fields, such as memristors.

Conclusion

To summarize, we have predicted a novel 2D layered semiconductor BaAs₃ that various exceptional electronic properties. The monolayered BaAs₃ is predicted to be an indirect semiconductor with a quite narrow band gap of 0.87 eV and can be tuned by controlling the layer thickness to cover a relatively large range of 0.87 eV to 0 eV, accordingly to shell GGA-1/2 calculations. The possibility of exfoliating layer BaAs₃ from the bulk structure has been confirmed by the 1.02 J m⁻² cleavage energy. The kinetic and thermal stability are verified by the phonon spectrum as well as AIMD simulations, proving that layered BaAs₃ can be produced as a freestanding 2D material in experiment. Meanwhile, monolayer and bilayer BaAs₃ also show outstanding carrier mobility for holes ($\sim 10^3$ cm² V⁻¹ s⁻¹). We find that the As₂ vacancy is easy to form in monolayer BaAs₃, which surprisingly leads to p-type conduction. On the other hand, the Ba vacancy is not effective in causing electrical conduction in monolayer BaAs₃. The special electronic properties of monolayer BaAs₃ may be useful for novel nanoelectronic devices.

ASSOCIATED CONTENT

Conflicts of interest

There are no conflicts to declare.

Acknowledgement

This work was supported by the National Key Research and Development Program of China (Materials Genome Initiative, 2017YFB0701700), the National Natural Science Foundation of China under Grant No. 11704134, and the Fundamental Research Funds of Wuhan City under Grant No. 2017010201010106. K.-H. Xue received support from China Scholarship Council (No. 201806165012).

REFERENCES

- [1] K.S. Novoselov, A.K. Geim, S.V. Morozov, D. Jiang, Y. Zhang, S.V. Dubonos, I.V. Grigorieva, A.A. Firsov, Electric Field Effect in Atomically Thin Carbon Films, *Science*. 306 (2004) 666–669. doi:10.1126/science.1102896.
- [2] B. Radisavljevic, A. Radenovic, J. Brivio, V. Giacometti, A. Kis, Single-layer MoS₂ transistors, *Nature Nanotechnology*. 6 (2011) 147–150. doi:10.1038/nnano.2010.279.
- [3] O. Lopez-Sanchez, D. Lembke, M. Kayci, A. Radenovic, A. Kis, Ultrasensitive photodetectors based on monolayer MoS₂, *Nature Nanotechnology*. 8 (2013) 497–501. doi:10.1038/nnano.2013.100.
- [4] C. Liu, Z. Yu, D. Neff, A. Zhamu, B.Z. Jang, Graphene-Based Supercapacitor with an Ultrahigh Energy Density, *Nano Letters*. 10 (2010) 4863–4868. doi:10.1021/nl102661q.
- [5] M.D. Stoller, S. Park, Y. Zhu, J. An, R.S. Ruoff, Graphene-Based Ultracapacitors, *Nano Letters*. 8 (2008) 3498–3502. doi:10.1021/nl802558y.
- [6] M.A. Lukowski, A.S. Daniel, F. Meng, A. Forticaux, L. Li, S. Jin, Enhanced Hydrogen Evolution Catalysis from Chemically Exfoliated Metallic MoS₂ Nanosheets, *Journal of the American Chemical Society*. 135 (2013) 10274–10277. doi:10.1021/ja404523s.
- [7] D. Deng, K.S. Novoselov, Q. Fu, N. Zheng, Z. Tian, X. Bao, Catalysis with two-dimensional materials and their heterostructures, *Nature Nanotechnology*. 11 (2016) 218–230. doi:10.1038/nnano.2015.340.
- [8] M.Z. Rahman, C.W. Kwong, K. Davey, S.Z. Qiao, 2D phosphorene as a water splitting photocatalyst: fundamentals to applications, *Energy & Environmental Science*. 9 (2016) 709–728. doi:10.1039/C5EE03732H.
- [9] J. Ran, B. Zhu, S.-Z. Qiao, Phosphorene Co-catalyst Advancing Highly Efficient Visible-Light Photocatalytic Hydrogen Production, *Angewandte Chemie International Edition*. 56 (2017) 10373–10377. doi:10.1002/anie.201703827.
- [10] L. Li, Y. Yu, G.J. Ye, Q. Ge, X. Ou, H. Wu, D. Feng, X.H. Chen, Y. Zhang, Black phosphorus field-effect transistors, *Nature Nanotechnology*. 9 (2014) 372–377.

- doi:10.1038/nnano.2014.35.
- [11] T. Fan, Y. Zhou, M. Qiu, H. Zhang, Black phosphorus: A novel nanoplatform with potential in the field of bio-photonic nanomedicine, *Journal of Innovative Optical Health Sciences*. (2018) 1830003. doi:10.1142/S1793545818300033.
- [12] X. Zhang, L. Hou, A. Ciesielski, P. Samorì 2D Materials Beyond Graphene for High-Performance Energy Storage Applications, *Advanced Energy Materials*. 6 (2016) 1600671. doi:10.1002/aenm.201600671.
- [13] J. Qiao, X. Kong, Z.-X. Hu, F. Yang, W. Ji, High-mobility transport anisotropy and linear dichroism in few-layer black phosphorus, *Nature Communications*. 5 (2014) 4475. doi:10.1038/ncomms5475.
- [14] N. Miao, B. Xu, N.C. Bristowe, J. Zhou, Z. Sun, Tunable Magnetism and Extraordinary Sunlight Absorbance in Indium Triphosphide Monolayer, *J. Am. Chem. Soc.* 139 (2017) 11125–11131. doi:10.1021/jacs.7b05133.
- [15] Y. Jing, Y. Ma, Y. Li, T. Heine, GeP₃: A Small Indirect Band Gap 2D Crystal with High Carrier Mobility and Strong Interlayer Quantum Confinement, *Nano Letters*. 17 (2017) 1833–1838. doi:10.1021/acs.nanolett.6b05143.
- [16] S. Sun, F. Meng, H. Wang, H. Wang, Y. Ni, Novel two-dimensional semiconductor SnP₃: high stability, tunable bandgaps and high carrier mobility explored using first-principles calculations, *Journal of Materials Chemistry A*. 6 (2018) 11890–11897. doi:10.1039/C8TA02494D.
- [17] J.-H. Yuan, A. Cresti, K.-H. Xue, Y.-Q. Song, H.-L. Su, L.-H. Li, N.-H. Miao, Z.-M. Sun, J.-F. Wang, X.-S. Miao, TIP₅: an unexplored direct band gap 2D semiconductor with ultra-high carrier mobility, *Journal of Materials Chemistry C*. (2019) 639-644. doi:10.1039/C8TC05164J.
- [18] N. Lu, Z. Zhuo, H. Guo, P. Wu, W. Fa, X. Wu, X.C. Zeng, CaP₃: A New Two-Dimensional Functional Material with Desirable Band Gap and Ultrahigh Carrier Mobility, *The Journal of Physical Chemistry Letters*. 9 (2018) 1728–1733. doi:10.1021/acs.jpcclett.8b00595.
- [19] F. Li, H. Wu, Z. Meng, R. Lu, Y. Pu, Tunable Topological State, High Hole-Carrier Mobility, and Prominent Sunlight Absorbance in Monolayered Calcium Triarsenide, *The Journal of Physical Chemistry Letters*. 10 (2019) 761–767. doi:10.1021/acs.jpcclett.9b00033.
- [20] Z. Liu, H. Wang, J. Sun, R. Sun, Z.F. Wang, J. Yang, Penta-Pt₂N₄: an ideal two-dimensional material for nanoelectronics, *Nanoscale*. 10 (2018) 16169–16177. doi:10.1039/C8NR05561K.
- [21] J.-H. Yuan, Y.-Q. Song, Q. Chen, K.-H. Xue, X.-S. Miao, Single-layer planar penta-X₂N₄ (X= Ni, Pd and Pt) as direct-bandgap semiconductors from first principle calculations, *Applied Surface Science*. (2018) 456-462. doi:10.1016/j.apsusc.2018.11.041.
- [22] H. Yuan, Z. Li, J. Yang, Atomically thin semiconducting penta-PdP₂ and PdAs₂ with ultrahigh carrier mobility, *Journal of Materials Chemistry C*. 6 (2018) 9055–9059. doi:10.1039/C8TC03368D.
- [23] J.-H. Yuan, B. Zhang, Y.-Q. Song, J.-F. Wang, K.-H. Xue, X.-S. Miao, Planar penta-transition metal phosphide and arsenide as narrow-gap semiconductors with ultrahigh carrier mobility, *Journal of Materials Science*. 54 (2019) 7035–7047. doi:10.1007/s10853-019-03380-4.
- [24] B. Ghosh, S. Puri, A. Agarwal, S. Bhowmick, SnP₃: A Previously Unexplored Two-Dimensional Material, *The Journal of Physical Chemistry C*. 122 (2018) 18185–18191. doi:10.1021/acs.jpcc.8b06668.

- [25] S. Yao, X. Zhang, Z. Zhang, A. Chen, Z. Zhou, 2D Triphosphides: SbP₃ and GaP₃ monolayer as promising photocatalysts for water splitting, *International Journal of Hydrogen Energy*. 44 (2019) 5948–5954. doi:10.1016/j.ijhydene.2019.01.106.
- [26] W. Bauhofer, M. Wittmann, H.G. v. Schnering, Structure, electrical and magnetic properties of CaAs₃, SrAs₃, BaAs₃ and EuAs₃, *Journal of Physics and Chemistry of Solids*. 42 (1981) 687–695. doi:10.1016/0022-3697(81)90122-0.
- [27] Q. Xu, R. Yu, Z. Fang, X. Dai, H. Weng, Topological nodal line semimetals in the CaP 3 family of materials, *Physical Review B*. 95 (2017) 045136. doi:10.1103/PhysRevB.95.045136.
- [28] G. Kresse, J. Furthmüller, Efficient iterative schemes for ab initio total-energy calculations using a plane-wave basis set, *Phys. Rev. B*. 54 (1996) 11169–11186. doi:10.1103/PhysRevB.54.11169.
- [29] G. Kresse, J. Furthmüller, Efficiency of ab-initio total energy calculations for metals and semiconductors using a plane-wave basis set, *Computational Materials Science*. 6 (1996) 15–50. doi:10.1016/0927-0256(96)00008-0.
- [30] J.P. Perdew, K. Burke, M. Ernzerhof, Generalized Gradient Approximation Made Simple, *Phys. Rev. Lett.* 77 (1996) 3865–3868. doi:10.1103/PhysRevLett.77.3865.
- [31] P.E. Blöchl, Projector augmented-wave method, *Phys. Rev. B*. 50 (1994) 17953–17979. doi:10.1103/PhysRevB.50.17953.
- [32] G. Kresse, D. Joubert, From ultrasoft pseudopotentials to the projector augmented-wave method, *Phys. Rev. B*. 59 (1999) 1758–1775. doi:10.1103/PhysRevB.59.1758.
- [33] A.V. Krukau, O.A. Vydrov, A.F. Izmaylov, G.E. Scuseria, Influence of the exchange screening parameter on the performance of screened hybrid functionals, *The Journal of Chemical Physics*. 125 (2006) 224106. doi:10.1063/1.2404663.
- [34] S. Grimme, J. Antony, S. Ehrlich, H. Krieg, A consistent and accurate *ab initio* parametrization of density functional dispersion correction (DFT-D) for the 94 elements H–Pu, *The Journal of Chemical Physics*. 132 (2010) 154104. doi:10.1063/1.3382344.
- [35] A. Togo, F. Oba, I. Tanaka, First-principles calculations of the ferroelastic transition between rutile-type and CaCl_2 -type SiO_2 at high pressures, *Phys. Rev. B*. 78 (2008) 134106. doi:10.1103/PhysRevB.78.134106.
- [36] G.J. Martyna, M.L. Klein, M. Tuckerman, Nosé–Hoover chains: The canonical ensemble via continuous dynamics, *The Journal of Chemical Physics*. 97 (1992) 2635–2643. doi:10.1063/1.463940.
- [37] K.-H. Xue, J.-H. Yuan, L.R.C. Fonseca, X.-S. Miao, Improved LDA-1/2 method for band structure calculations in covalent semiconductors, *Computational Materials Science*. 153 (2018) 493–505. doi:10.1016/j.commatsci.2018.06.036.
- [38] L.G. Ferreira, M. Marques, L.K. Teles, Approximation to density functional theory for the calculation of band gaps of semiconductors, *Phys. Rev. B*. 78 (2008) 125116. doi:10.1103/PhysRevB.78.125116.
- [39] J.-H. Yuan, Q. Chen, L.R. Fonseca, M. Xu, K. Xue, X. Miao, GGA-1/2 self-energy correction for accurate band structure calculations: the case of resistive switching oxides, *Journal of Physics Communications*. (2018) 105065. doi:10.1088/2399-6528/aade7e.
- [40] C. Kamal, M. Ezawa, Arsenene: Two-dimensional buckled and puckered honeycomb arsenic systems, *Physical Review B*. 91 (2015). doi:10.1103/PhysRevB.91.085423.
- [41] W. Wang, S. Dai, X. Li, J. Yang, D.J. Srolovitz, Q. Zheng, Measurement of the cleavage

- energy of graphite, *Nature Communications*. 6 (2015) 7853.
- [42] Y.-Q. Song, J.-H. Yuan, L.-H. Li, M. Xu, J.-F. Wang, K.-H. Xue, X.-S. Miao, KTlO: a metal shrouded 2D semiconductor with high carrier mobility and tunable magnetism, *Nanoscale*. (2019) 1131-1139. doi:10.1039/C8NR08046A.
- [43] A. Savin, R. Nesper, S. Wengert, T.F. Fässler, ELF: The Electron Localization Function, *Angewandte Chemie International Edition in English*. 36 (1997) 1808–1832. doi:10.1002/anie.199718081.
- [44] A.D. Becke, K.E. Edgecombe, A simple measure of electron localization in atomic and molecular systems, *The Journal of Chemical Physics*. 92 (1990) 5397–5403. doi:10.1063/1.458517.
- [45] W. Tang, E. Sanville, G. Henkelman, A grid-based Bader analysis algorithm without lattice bias, *Journal of Physics: Condensed Matter*. 21 (2009) 084204. doi:10.1088/0953-8984/21/8/084204.
- [46] G. Henkelman, A. Arnaldsson, H. Jónsson, A fast and robust algorithm for Bader decomposition of charge density, *Computational Materials Science*. 36 (2006) 354–360. doi:10.1016/j.commatsci.2005.04.010.
- [47] E. Sanville, S.D. Kenny, R. Smith, G. Henkelman, Improved grid-based algorithm for Bader charge allocation, *Journal of Computational Chemistry*. 28 (2007) 899–908. doi:10.1002/jcc.20575.
- [48] J. Bardeen, W. Shockley, Deformation Potentials and Mobilities in Non-Polar Crystals, *Physical Review*. 80 (1950) 72–80. doi:10.1103/PhysRev.80.72.
- [49] H. Lang, S. Zhang, Z. Liu, Mobility anisotropy of two-dimensional semiconductors, *Physical Review B*. 94 (2016) 235306. doi:10.1103/PhysRevB.94.235306.
- [50] M. Zhou, X. Chen, M. Li, A. Du, Widely tunable and anisotropic charge carrier mobility in monolayer tin(II) selenide using biaxial strain: a first-principles study, *Journal of Materials Chemistry C*. 5 (2017) 1247–1254. doi:10.1039/C6TC04692D.
- [51] C.G. Van de Walle, J. Neugebauer, First-principles calculations for defects and impurities: Applications to III-nitrides, *Journal of Applied Physics*. 95 (2004) 3851–3879. doi:10.1063/1.1682673.

Supporting Information for

BaAs₃: A narrow gap 2D semiconductor with vacancy-induced semiconductor-metal transition

Ping Tang,¹⁺ Jun-Hui Yuan,¹⁺ Ya-Qian Song,¹ Ming Xu,¹ Kan-Hao Xue,^{1,2*} Xiang-Shui Miao¹

¹ Wuhan National Research Center for Optoelectronics, School of Optical and Electronic Information, Huazhong University of Science and Technology, Wuhan 430074, China

² Univ. Grenoble Alpes, Univ. Savoie Mont Blanc, CNRS, Grenoble INP, IMEP-LAHC, 38000 Grenoble, France

⁺The authors P. Tang and J.-H. Yuan contributed equally to this work.

Corresponding Author

*E-mail: xkh@hust.edu.cn (K.-H. Xue)

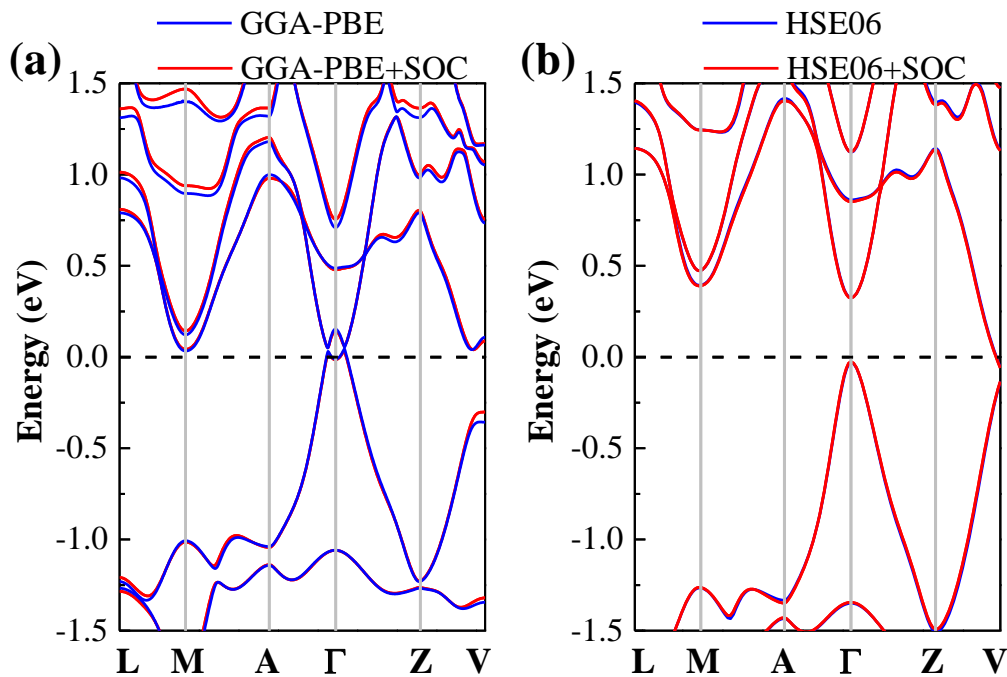


Figure S1. (a) Band structures of bulk BaAs₃ calculated using the PBE functional, either with or without considering the effect of spin orbit coupling (SOC). (b) Band structures of bulk BaAs₃ calculated using the screened exchange HSE06 hybrid functional, either with or without considering the effect of SOC.

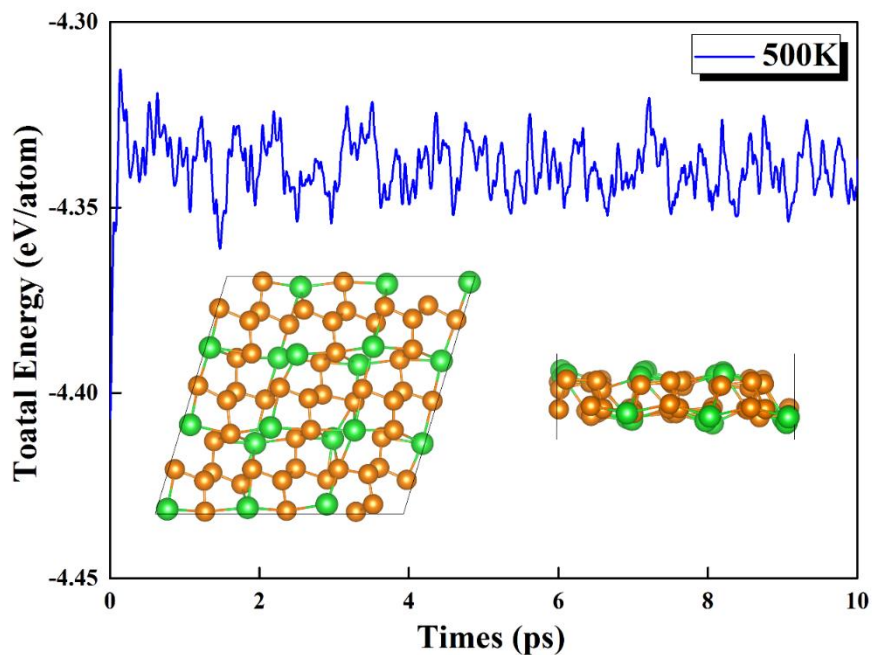


Figure S2. Top and side views of a snapshot from the molecules dynamics simulation for the ML BaAs₃. The variation of total energy is recorded and demonstrated over the simulation time of 10 ps, while the temperature was 500 K.

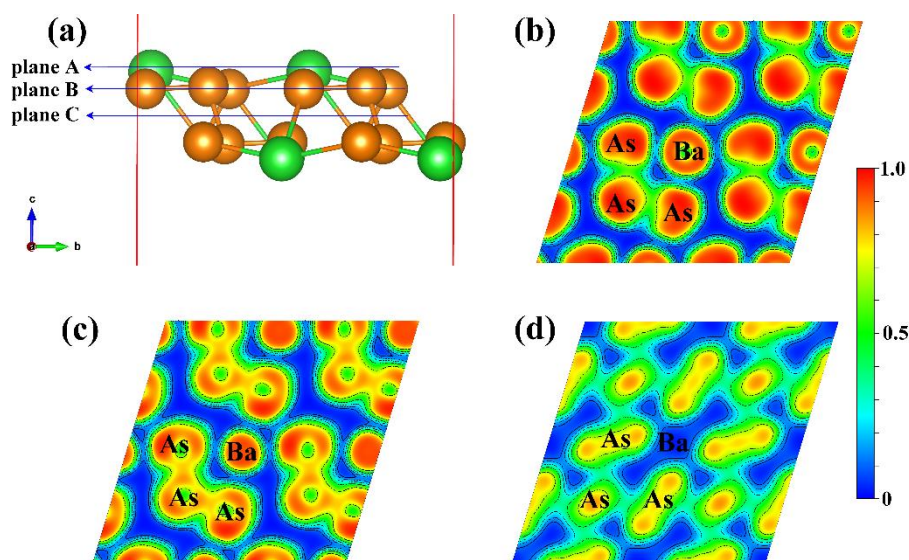


Figure S3. (a) Side view of ML BaAs₃ with planes A/B/C marked. Electron localization functions (ELFs) of: (b) plane A, (c) plane B, and (d) plane C, respectively.

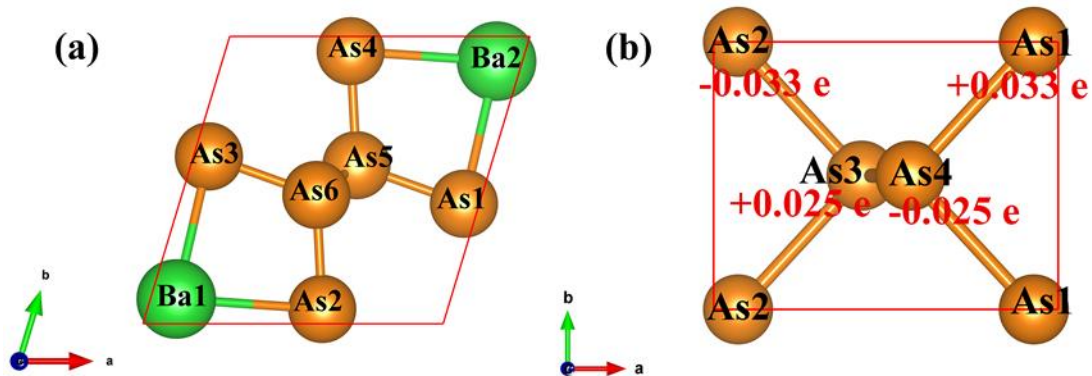


Figure S4. (a) Top view of ML BaAs₃ with all atoms marked by element symbol and numbers. (b) Top view of puckered arsenene with Bader charge values marked.

Table S1. Charge transfer between Ba and As atoms in ML BaAs₃ according to the Bader gauge. Here “+” and “-” represent a loss and a gain of electrons, respectively.

	Ba1	Ba2	As1	As2	As3	As4	As5	As6
Charge (e)	+1.3186	+1.3186	-0.5614	-0.5723	-0.5680	-0.5720	-0.1794	-0.1843

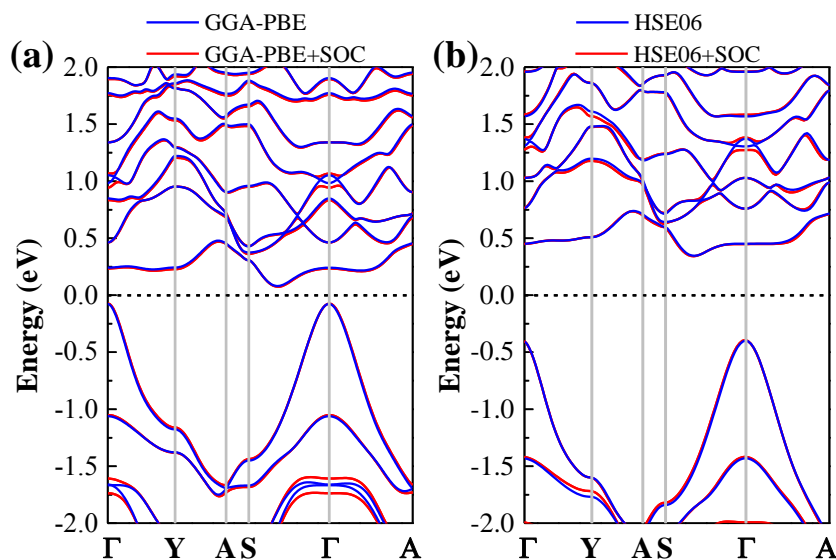


Figure S5. (a) Band structures of ML BaAs₃ calculated using the PBE functional, either with or without considering the effect of spin orbit coupling (SOC). (b) Band structures of ML BaAs₃ calculated using the screened exchange HSE06 hybrid functional, either with or without considering the effect of SOC.

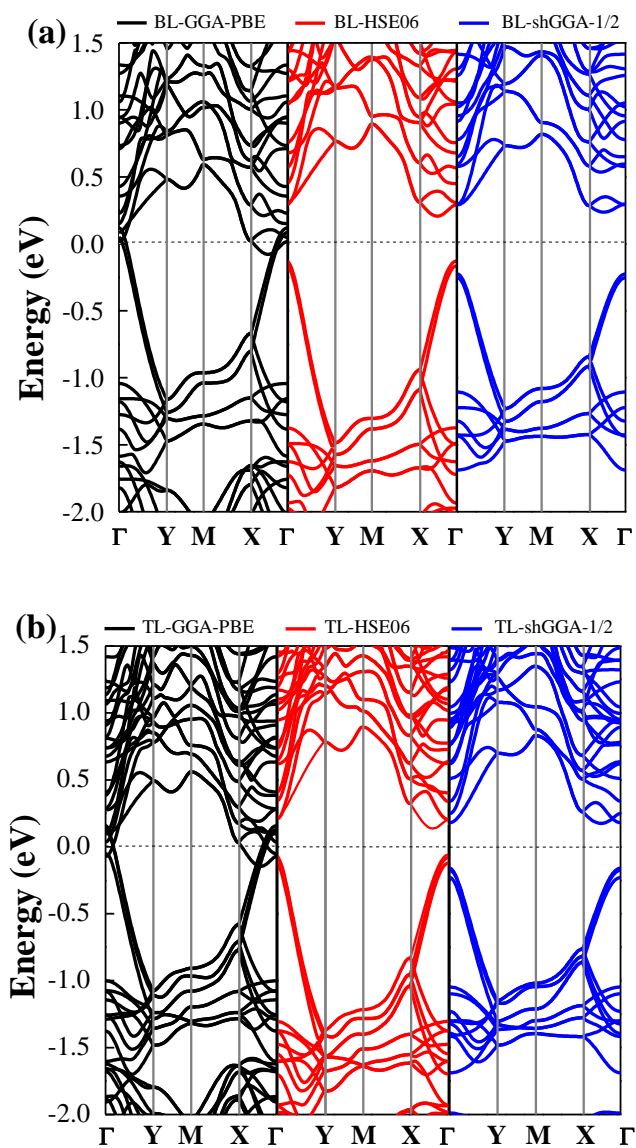


Figure S6. Electronic band structures of 2D BaAs₃ with varying number of layers, calculated using GGA-PBE, HSE06 hybrid functional and the shGGA-1/2 method: (a) bilayer (BL for short); (b) trilayer (TL for short).

Table S2. The optimized lattice constants ($a/b/c$) in ML BaAs₃, BL, TL and bulk, respectively, in comparison to the experimental bulk values (Exp.).

Lattice constant	ML	BL	TL	Bulk	Exp. ¹
$a/\text{\AA}$	6.51	10.27	10.26	10.22	11.16
$b/\text{\AA}$	6.25	7.80	7.81	7.82	7.76
$c/\text{\AA}$	--	--	--	6.06	6.01
$\alpha/^\circ$	89.76	90	90	90	90
$\beta/^\circ$	89.76	90.07	106.40	113.70	113.55
$\gamma/^\circ$	73.19	90	90	90	90

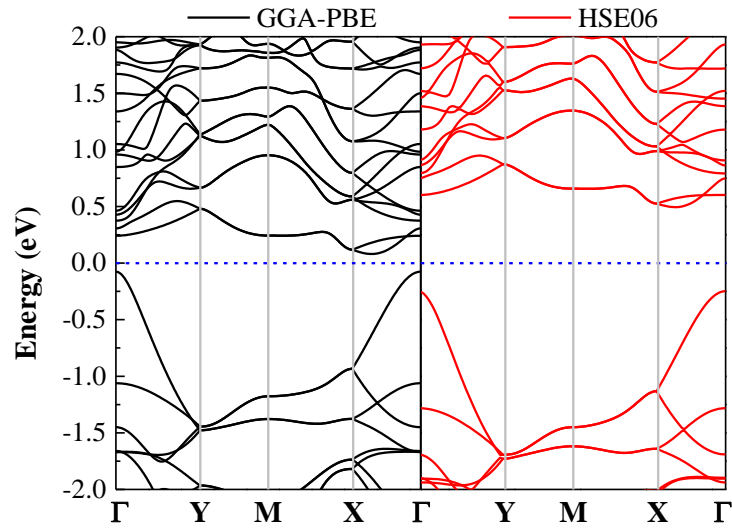


Figure S7. Electronic band structures of ML BaAs₃ in an orthogonal supercell, calculated using both GGA-PBE and the screened exchange HSE06 hybrid functional.

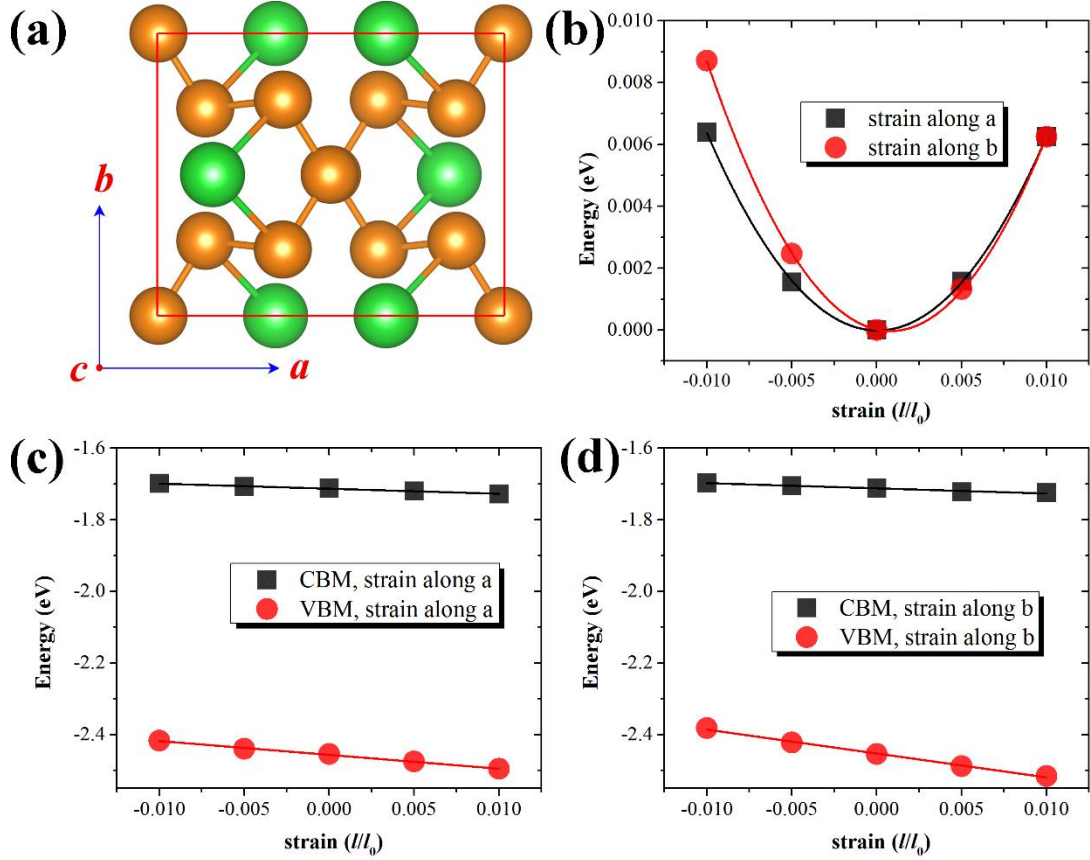


Figure S8. (a) The orthogonal supercell of ML BaAs₃. (b) The relation between total energy and the applied strain δ along the *a* and *b* directions of ML BaAs₃. The quadratic data fitting gives the in-plane stiffness of 2D structures. Black and red curves show the in-plane stiffness along the *a* and *b* directions of ML BaAs₃, respectively. (c) The shift of VBM and CBM for ML BaAs₃ with respect to the vacuum energy, as a function of the applied strain along the *a* direction. (d) The shift of VBM and CBM for ML BaAs₃ with respect to the vacuum energy, as a function of the applied strain along the *b* direction. The linear fit of the data yields the deformation potential constant. All the calculations were based on the HSE06 functional.

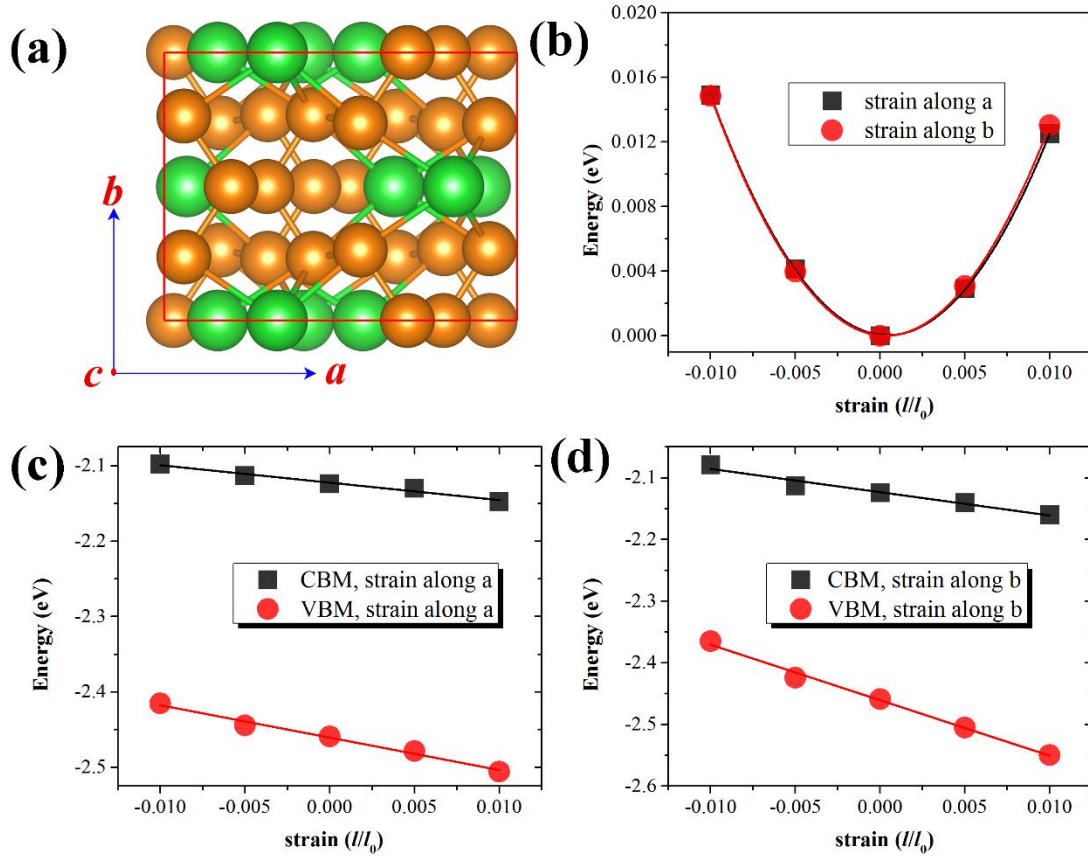


Figure S9. (a) The orthogonal supercell of bilayer BaAs₃. (b) The relation between total energy and the applied strain δ along the a and b directions of bilayer BaAs₃. The quadratic data fitting gives the in-plane stiffness of 2D structures. Black and red curves show the in-plane stiffness along the a and b directions of bilayer BaAs₃, respectively. (c) The shift of VBM and CBM for bilayer BaAs₃ with respect to the vacuum energy, as a function of the applied strain along the a direction. (d) The shift of VBM and CBM for bilayer BaAs₃ with respect to the vacuum energy, as a function of the applied strain along the b direction. The linear fit of the data yields the deformation potential constant. All the calculations were based on the HSE06 functional.

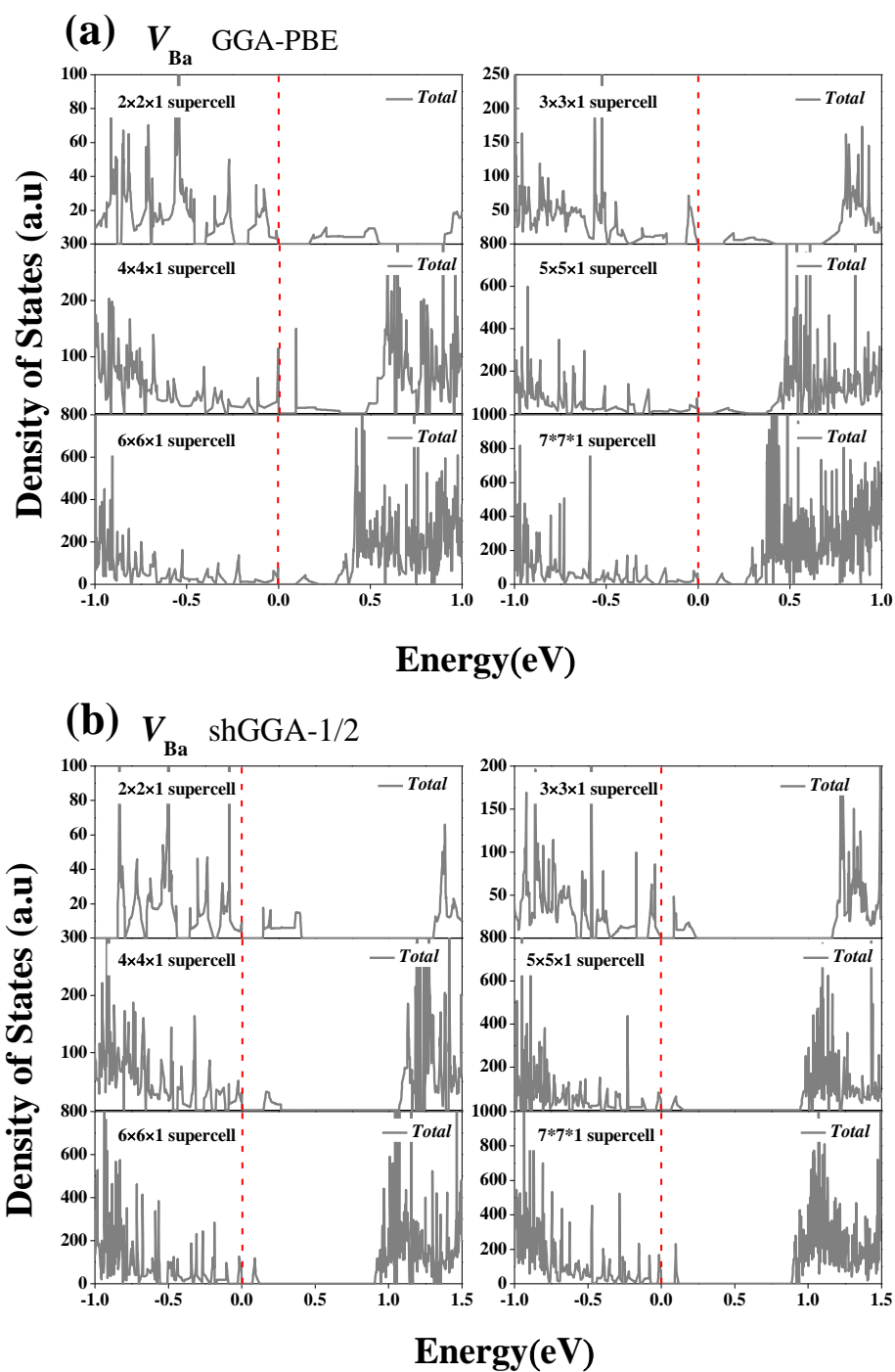


Figure S10. Partial DOS of V_{Ba} -containing supercells from $2 \times 2 \times 1$ to $7 \times 7 \times 1$, calculated using (a) the GGA-PBE functional; (b) the shGGA-1/2 method.

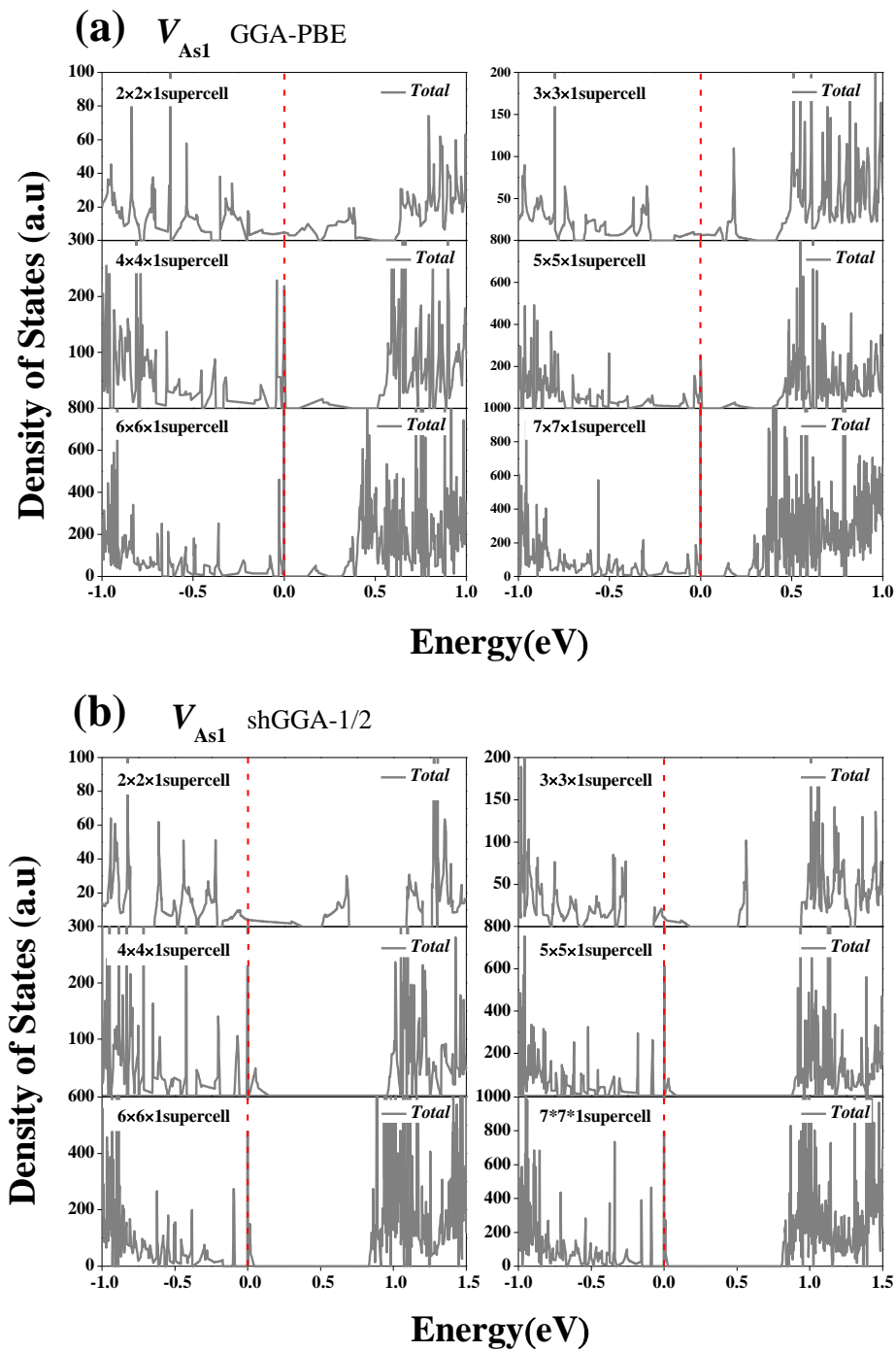


Figure S11. Partial DOS of V_{As1} -containing supercells from $2 \times 2 \times 1$ to $7 \times 7 \times 1$, calculated using (a) the GGA-PBE functional; (b) the shGGA-1/2 method.

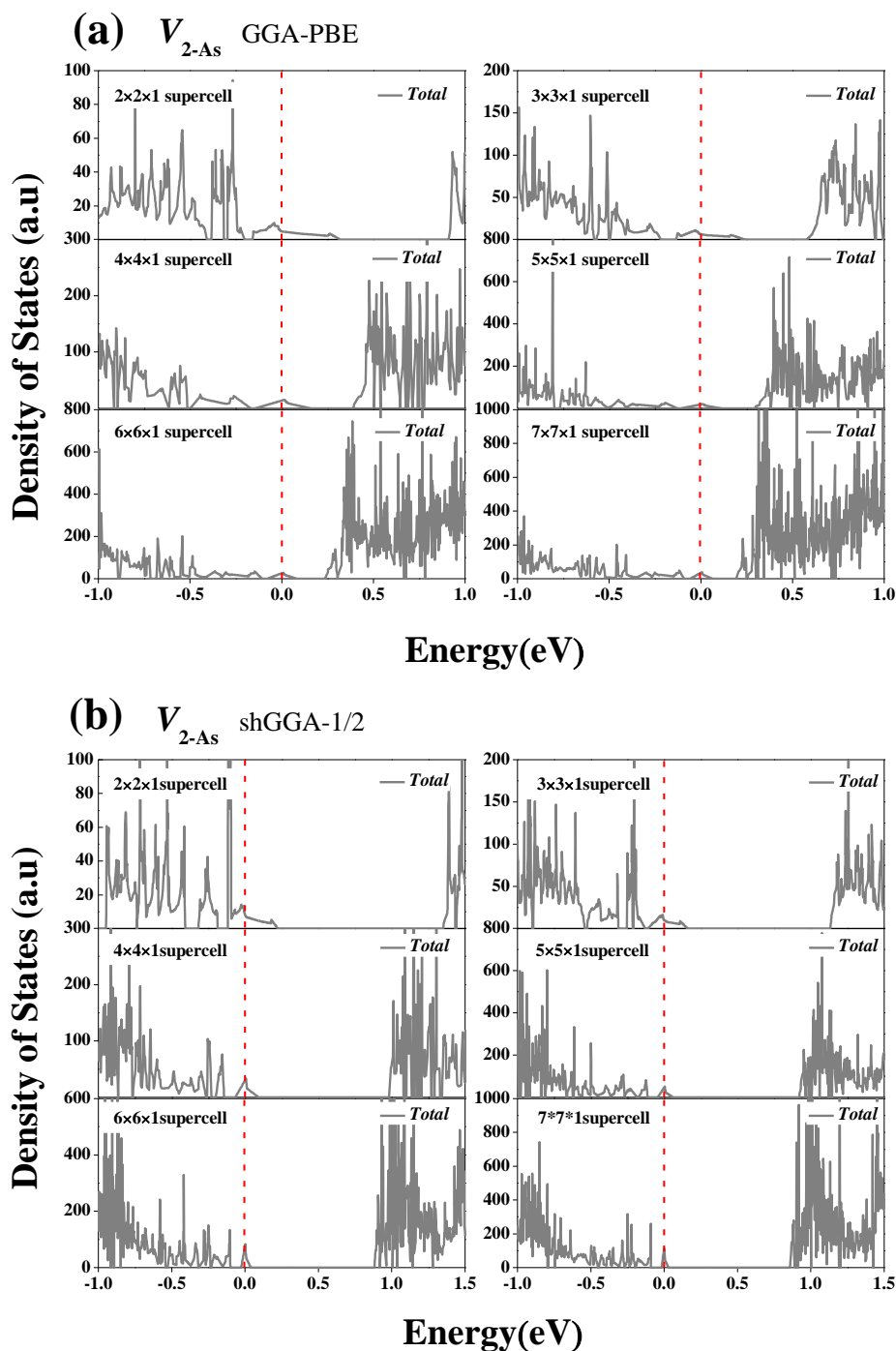


Figure S12. Partial DOS of V_{As2} -containing supercells from $2 \times 2 \times 1$ to $7 \times 7 \times 1$, calculated using (a) the GGA-PBE functional; (b) the shGGA-1/2 method.

REFERENCES

- (1) Bauhofer, W.; Wittmann, M.; Schnering, H. G. v. Structure, Electrical and Magnetic Properties of $CaAs_3$, $SrAs_3$, $BaAs_3$ and $EuAs_3$. *Journal of Physics and Chemistry of Solids* **1981**, 42 (8), 687–695. [https://doi.org/10.1016/0022-3697\(81\)90122-0](https://doi.org/10.1016/0022-3697(81)90122-0).